Int. J. Heat Mass Transfer. Vol. 35, No. 1, pp. 239–254, 1992
Printed in Great Britain

0017-9310/92 $5.00+0.00

Simultaneously developing laminar convection in rotating isothermal square channels

TIEN-CHIEN JEN and ADRIENNE S. LAVINE
Mechanical, Aerospace and Nuclear Engineering Department, University of California,
Los Angeles, CA 90024-1597, U.S.A.

and

GUANG-JYH HWANG
Department of Power Mechanical Engineering, National Tsing Hua University, Hsinchu,
Taiwan, China

(*Received* 21 *September* 1990 *and in final form* 15 *January* 1991)

Abstract—A numerical analysis is conducted on laminar forced convection in the entrance region of an isothermal square duct rotating about an axis perpendicular to the duct axis. The simultaneously developing flow case is examined. Three independent parameters are introduced: Prandtl number (Pr), a combined Reynolds and rotational Reynolds number ($Re\ Re_{\Omega}$), and Rossby number (Ro). A relatively novel vorticity–velocity method along with the power law scheme is employed in the present numerical analysis. Typical developments of axial velocity, secondary flow, and temperature at various axial positions in the entrance region are presented. Local friction factor and Nusselt number variations are reported. A comparison of the numerical results with the available experimental data is also presented.

INTRODUCTION

HEAT TRANSFER and fluid flow in rotating channels are important subjects encountered in many engineering applications, for example, in the rotors of electrical machinery, gas turbines, and many other rotating machinery. Research on heat transfer in rotating pipes has intensified with the aim of raising the operating temperature of gas turbines. Many investigators have studied flow and heat transfer characteristics in rotating ducts. A detailed literature review for rotating ducts is given in refs. [1, 2]. Some particularly relevant papers are reviewed here. The laminar flow and heat transfer problem in rectangular ducts was studied in refs. [1–3]. The friction factor and Nusselt number were reported for a large range of parameters, and showed qualitative agreement with experiment. Hart [4] employed linear stability analysis for the laminar flow regime, and made experimental measurements of critical conditions required for the onset of instabilities. Lezius and Johnston [5] analyzed the Taylor-type roll cell instability for the laminar and turbulent flow in a rotating parallel plate channel. A numerical analysis of the fully developed region in a rotating isothermal isosceles triangular duct with three different aspect ratios is presented in ref. [6]. Spezial *et al.* [7–9] studied the laminar flow in rotating rectangular ducts extensively. For constant axial pressure gradient, they calculated the velocities and showed the flow pattern qualitatively. Smirnov [10] computed the laminar flow in rotating rectangular ducts of aspect ratios 1 and 2 numerically. The friction factors and marginal stability curve were obtained.

The earlier works mostly concentrated on the hydrodynamically and thermally fully developed region. Reports of developing flows are very rare [11]. The available entrance region data from both theoretical and experimental studies are now reviewed. Metzger and Stan [12] investigated experimentally the effect of rotation on the entrance region heat transfer inside straight, circular tubes. Skiadaressis and Spalding [13] predicted the flow and the heat transfer characteristics for turbulent steady flow in rectangular ducts using the k–ε model. Recently, heat transfer measurements were carried out in a rotating isothermal square duct for Reynolds numbers ranging from 717 to 16 000 and rotational Reynolds numbers from 20 to 320 [14], and in rectangular ducts for aspect ratios of 0.2, 0.5, 1, 2, and 5 [15].

It is noted that there are no numerical studies for the laminar entrance region, particularly in rectangular ducts. In practical applications, the flow typically remains thermally developing for almost the full length of the duct. Furthermore, rectangular channels are more appropriate than triangular or circular ducts for the central portion of a turbine blade [14]. For these reasons, this study addresses the simultaneously developing flow in a square rotating channel. The channel wall is heated with a constant wall temperature. The non-linear parabolized Navier–Stokes equations are solved by the vorticity–velocity method along with the power law scheme [16]. The vorticity–

NOMENCLATURE

A	cross-sectional area
D_e	hydraulic diameter, $4A/S$
f	friction factor, $\bar{\tau}_w/\frac{1}{2}\rho\bar{W}^2$
Nu	peripherally averaged Nusselt number
K	Dean number
n	dimensionless normal direction coordinate
P, p	pressure and dimensionless pressure
Pr	Prandtl number, ν/α
Re	Reynolds number, $\bar{W}D_e/\nu$
Re_Ω	rotational Reynolds number, $\Omega D_e^2/\nu$
Ro	Rossby number, $Re/2Re_\Omega$
S	perimeter
T	temperature
U, V, W	velocity components in the X-, Y-, Z-directions
u, v, w	dimensionless velocity components in the x-, y-, z-directions
X, Y, Z	rectangular coordinates
x, y, z	dimensionless rectangular coordinates.

Greek symbols

α	thermal diffusivity of fluid
θ	dimensionless temperature defined in equation (5)
ν	kinematic viscosity
ξ	vorticity defined in equation (11)
ρ	density
τ_w	wall shear stress
Ω	angular speed.

Subscripts

c	characteristic quantity
in	inlet quantity
m	bulk mean quantity
o	condition without rotation
w	condition at wall.

velocity method was successfully employed in refs. [17–19] to calculate three-dimensional natural and mixed convection problems in rectangular and cylindrical ducts. The advantages of the vorticity–velocity method were indicated by Spezial [20], and present calculations also indicate that this method is as effective as the primitive variables method [21]. The results obtained from the computations cover a broad range of parameters, especially from low rotational speed to high rotational speed, with $Pr = 0.7$ and 7.0. The Nusselt number, friction factor, velocity profile, secondary flow patterns, and isotherm maps in the entrance region are presented.

THEORETICAL ANALYSIS

Consider the steady, laminar, developing forced convection flow in an isothermal square channel rotating at a constant angular speed about an axis perpendicular to the channel longitudinal direction as shown in Fig. 1. A uniform inlet axial velocity $W_{in} = \bar{W}$ and a constant inlet temperature T_{in} are imposed at $Z = 0$. The duct wall temperature is held constant at T_w. The flow is assumed to be steady, have constant property, and be incompressible; axial diffusion, viscous dissipation, compression work, and buoyancy are neglected. Note that the centrifugal-buoyancy effect may not be negligible when the Reynolds number is less than or of the same order as the rotational Reynolds number (i.e. $Ro < 0.5$). However, this effect is neglected in the present calculations. It was shown in refs. [1–3] that the axial heat diffusion term is negligible in rotating duct flow when the Peclet number is greater than about 10.

A modified pressure P, which includes the centrifugal force, may be defined as

$$P(X, Y, Z) = \bar{P}(Z) + P^*(X, Y, Z) + \tfrac{1}{2}\rho Z^2\Omega^2 \quad (1)$$

where $\bar{P}(Z)$ is the pressure averaged over the cross section at each axial location, and $P^*(X, Y, Z)$ is the pressure variation in the cross-stream direction which drives the secondary flow. Defining

$$\bar{P}^*(Z) = \bar{P}(Z) + \tfrac{1}{2}\rho Z^2\Omega^2 \quad (2)$$

then the modified pressure in equation (1) is

$$P(X, Y, Z) = \bar{P}^*(Z) + P^*(X, Y, Z) \quad (3)$$

or in non-dimensional form (as defined in equation (5), below)

$$p(x, y, z) = \bar{p}^*(z) + p^*(x, y, z).$$

So far, no approximations have been made. Now, the axial and cross-sectional pressure gradients may be decoupled by making the usual parabolic assumption [22], that $\partial p^*/\partial z \ll \mathrm{d}\bar{p}^*/\mathrm{d}z$. The axial pressure gradient is then given by

$$-\frac{\partial p}{\partial z} = -\frac{\mathrm{d}\bar{p}^*}{\mathrm{d}z} = -f(z) \quad (4)$$

where $f(z)$ is determined by the constant flow rate constraint.

The following dimensionless variables and parameters are introduced:

$$x = \frac{X}{D_e},\quad y = \frac{Y}{D_e},\quad z = \frac{Z}{Re\,D_e},\quad u = \frac{U}{U_c},\quad v = \frac{V}{U_c}$$

$$w = \frac{W}{W_c},\quad p = \frac{P}{P_c},\quad p^* = \frac{P^*}{P_c},\quad \bar{p}^* = \frac{\bar{P}^*}{P_c}$$

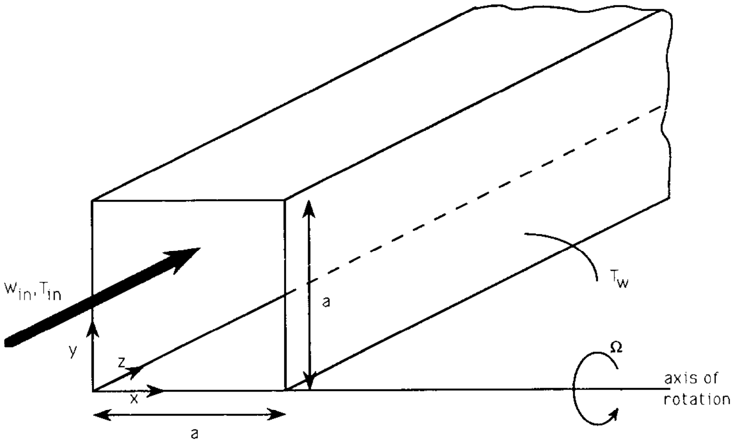

FIG. 1. Physical configuration and coordinate system.

$$\theta = \frac{(T-T_w)}{(T_{in}-T_w)}, \quad Re = \frac{\bar{W}D_e}{\nu}, \quad Re_\Omega = \frac{\Omega D_e^2}{\nu}$$

$$Pr = \frac{\nu}{\alpha}, \quad Ro = \frac{Re}{2Re_\Omega} = \frac{\bar{W}}{2\Omega D_e} \tag{5}$$

where

$$P_c = \rho\, Re\, Re_\Omega \left(\frac{\nu}{D_e}\right)^2, \quad U_c = Re\, Re_\Omega \left(\frac{\nu}{D_e}\right)$$

$$W_c = \bar{W}\, Re\, Re_\Omega, \quad D_e = \frac{4A}{S}.$$

The dimensionless governing equations can then be written as follows:

$$\frac{\partial u}{\partial x} + \frac{\partial v}{\partial y} + \frac{\partial w}{\partial z} = 0 \tag{6}$$

$$Re\, Re_\Omega \left(u\frac{\partial u}{\partial x} + v\frac{\partial u}{\partial y} + w\frac{\partial u}{\partial z}\right) = -\frac{\partial p^*}{\partial x} + \frac{\partial^2 u}{\partial x^2} + \frac{\partial^2 u}{\partial y^2} \tag{7}$$

$$Re\, Re_\Omega \left(u\frac{\partial v}{\partial x} + v\frac{\partial v}{\partial y} + w\frac{\partial v}{\partial z}\right) = -\frac{\partial p^*}{\partial y} + \frac{\partial^2 v}{\partial x^2} + \frac{\partial^2 v}{\partial y^2} - 2Re\, Re_\Omega\, w \tag{8}$$

$$Re\, Re_\Omega \left(u\frac{\partial w}{\partial x} + v\frac{\partial w}{\partial y} + w\frac{\partial w}{\partial z}\right) = -f(z) + \frac{\partial^2 w}{\partial x^2} + \frac{\partial^2 w}{\partial y^2} + \frac{v}{Ro} \tag{9}$$

$$Pr\, Re\, Re_\Omega \left(u\frac{\partial \theta}{\partial x} + v\frac{\partial \theta}{\partial y} + w\frac{\partial \theta}{\partial z}\right) = \frac{\partial^2 \theta}{\partial x^2} + \frac{\partial^2 \theta}{\partial y^2}. \tag{10}$$

The solution depends on three independent parameters: Prandtl number (*Pr*), a combined Reynolds and rotational Reynolds number ($Re\, Re_\Omega$), and Rossby number (*Ro*).

The term $2Re\, Re_\Omega\, w$ on the right-hand side of equation (8) is the Coriolis force driving the flow in the negative y-direction. The term v/Ro in equation (9) is also the Coriolis force from the product of the y-direction secondary flow velocity and the angular velocity. This force may act locally in either the upstream or downstream direction, depending on the sign of v.

From equations (6) to (10), one can find that the rotational effects are characterized by two dimensionless groups $Ro = Re/2Re_\Omega$ and $Re\, Re_\Omega$. Physically, the former represents the ratio of the inertia force to the Coriolis force or the relative significance of the forced flow effect to the Coriolis-induced secondary flow effect, and the latter is a combination of the axial velocity $\bar{W}$ and the angular speed Ω indicating the effect of the Coriolis force.

Different scaling quantities used in the nondimensionalization may generate different parameter groups for the rotating effects. For example, *Re* and *Ro* are obtained if all the velocity components are nondimensionalized by using $\bar{W}$ as a reference; $Re\, Re_\Omega$ and *Ro* are obtained if ν/D_e is used for U and V, and $\bar{W}$ for W. The advantage of using $Re\, Re_\Omega$ is that, at large *Ro*, the secondary flow induced Coriolis force effect may be negligible (i.e. last term of equation (9)), thus the one parameter $Re\, Re_\Omega$ can represent the behavior of a rotating duct instead of two parameters (i.e. *Re* and *Ro*), which was demonstrated in ref. [1]. In traditional turbine cooling blade systems, *Re* and *Ro* are used, however these two parameter values are easy to recover from the present analysis.

The equations are now put into the vorticity–velocity form. The axial vorticity function is defined as

$$\xi = \frac{\partial u}{\partial y} - \frac{\partial v}{\partial x}. \tag{11}$$

Applied to the continuity equation, this yields

$$\nabla^2 u = \frac{\partial \xi}{\partial y} - \frac{\partial^2 w}{\partial x \partial z} \tag{12}$$

$$\nabla^2 v = -\frac{\partial \xi}{\partial x} - \frac{\partial^2 w}{\partial y\, \partial z}. \qquad (13)$$

Cross differentiation of the x and y momentum equations to eliminate cross-sectional pressure terms yields

$$Re\, Re_\Omega \left[u\frac{\partial \xi}{\partial x} + v\frac{\partial \xi}{\partial y} + w\frac{\partial \xi}{\partial z} + \xi\left(\frac{\partial u}{\partial x} + \frac{\partial v}{\partial y}\right) + \left(\frac{\partial w}{\partial y}\frac{\partial u}{\partial z} - \frac{\partial w}{\partial x}\frac{\partial v}{\partial z}\right)\right] = \frac{\partial^2 \xi}{\partial x^2} + \frac{\partial^2 \xi}{\partial y^2} + 2Re\, Re_\Omega \frac{\partial w}{\partial x}. \qquad (14)$$

An additional constraint which will be used to determine $f(z)$ is that global mass conservation must be satisfied. Defining a different non-dimensional axial velocity, w_t, for convenience, this constraint is expressed as

$$\bar{w}_t = \int_0^1 \int_0^1 w_t \, dx \, dy = 1.0 \qquad (15)$$

where

$$w_t = \frac{W}{\bar{W}} = w\, Re\, Re_\Omega.$$

The boundary conditions are:

$$u = v = w = \theta = 0 \quad \text{at walls}$$

$$u = v = \xi = 0, \quad \text{and} \quad w_t = \theta = 1 \quad \text{at} \quad z = 0. \qquad (16)$$

After the developing velocity and temperature fields are obtained, the computations of the local friction factor and Nusselt number are of practical interest. Following the usual definitions, the expression for the product of the peripherally averaged friction factor and Reynolds number, $f\,Re$, and the peripherally averaged Nusselt number, Nu, can be written based on the axial velocity gradient or the temperature gradient at the wall, or based on the overall force or energy balance for an axial length dZ. The expressions are

$$(f\,Re)_1 = 2\overline{\left(\frac{\partial w_t}{\partial n}\right)}_{\text{wall}} \qquad (17)$$

$$(f\,Re)_2 = -Re\, Re_\Omega \frac{f(z)}{2} + \frac{Re\, Re_\Omega}{2Ro} \int_0^1 \int_0^1 v \, dx \, dy - \frac{1}{2}\int_0^1 \int_0^1 \frac{\partial w_t^2}{\partial z} \, dx \, dy. \qquad (18)$$

The local Nusselt numbers are

$$(Nu)_1 = \frac{1}{\theta_m}\overline{\left(\frac{\partial \theta}{\partial n}\right)}_{\text{wall}} \qquad (19)$$

$$(Nu)_2 = \frac{1}{\theta_m}\frac{Pr}{S}\int_0^1 \int_0^1 \frac{\partial w_t \theta}{\partial z} \, dx \, dy \qquad (20)$$

where the overbar in equations (17) and (19) means the average around the perimeter, and S is the perimeter of the duct. Simpson's 3/8 rule is used to compute the average quantities indicated above. The quantity θ_m is defined as

$$\theta_m = \frac{(T_m - T_w)}{(T_{in} - T_w)} = \int_0^1 \int_0^1 w_t \theta \, dx \, dy \qquad (21)$$

where T_m is the mean temperature.

The calculated quantities $(f\,Re)_1$ and $(f\,Re)_2$ were found to be in excellent agreement (within 1%) for $z > 3.7 \times 10^{-4}$. The quantity $(f\,Re)_2$ is used throughout the present study. The quantities $(Nu)_1$ and $(Nu)_2$ were also in good agreement (within 1%) for $z/Pr > 3.17 \times 10^{-3}$. Due to the better agreement with the previous calculations [1, 2] in the fully developed region, $(Nu)_1$ is adopted throughout the present numerical analysis.

METHOD OF SOLUTION

The governing equations are solved numerically by the vorticity–velocity method for three-dimensional parabolic flow, along with the power law scheme [16].

The equations for the unknowns u, v, w, ξ, θ, and $f(z)$, equations (12)–(15), (9), and (10), satisfying boundary conditions (16) are coupled. A numerical finite-difference scheme based on the vorticity–velocity method is developed in this paper to obtain the solution of equations (12)–(15), (9), and (10). The procedure is as follows:

(1) The initial values of the unknowns u, v, and ξ are assigned to be zero at the entrance, $z = 0$. Uniform inlet axial velocity (i.e. $w_t = 1$) and inlet temperature (i.e. $\theta = 1$) are used. Note that $\xi = 0$ at $z = 0$ results from equation (11). It is noted that this procedure can be extended to any kind of inlet velocity profile, so that this numerical scheme is flexible.

(2) In equation (14), the values of $\partial w/\partial x$, $\partial w/\partial y$, $\partial u/\partial x$, and $\partial v/\partial y$, at each grid point are easily obtained by using central differencing. The values of $\partial u/\partial z$ and $\partial v/\partial z$ are computed by using a two-point backward differencing.

(3) By using the known values of u, v, w, ξ, and $f(z)$ at the present position, the new values of ξ, w, and $f(z)$ at the interior points of the next axial position are obtained from equations (14) and (9), respectively, by the power law scheme [16], with constraint (15) to meet the requirement of constant flow rate.

(4) The values of $\partial^2 w/\partial x \partial z$, $\partial^2 w/\partial y \partial z$, $\partial \xi/\partial y$, and $\partial \xi/\partial x$, in equations (12) and (13) are calculated by using backward differences axially and central difference in the transverse directions. The elliptic-type equations (12) and (13) are then solved for u and v by iteration. During the iteration process, the values of vorticity on the boundary are evaluated simultaneously with u and v in the interior region. The boundary vorticity can be evaluated with an expression given in ref. [18].

(5) Steps 2–4 are repeated at a cross section until the following convergence criterion is satisfied for the velocity components u and v:

$$\varepsilon = \frac{\max |u_{i,j}^{n+1} - u_{i,j}^{n}|}{\max |u_{i,j}^{n+1}|} < 10^{-5} \tag{22}$$

where n is the nth iteration of steps 2–4.

(6) The peripherally averaged $f\ Re$ are calculated from equations (17) and (18).

(7) With the obtained solutions for u, v, and w, equation (10) can be solved iteratively for the interior temperature subject to the boundary condition $\theta = 0$. This step is repeated until the following convergence criterion is satisfied:

$$\varepsilon = \frac{\max |\theta_{i,j}^{m+1} - \theta_{i,j}^{m}|}{\max |\theta_{i,j}^{m+1}|} < 10^{-6} \tag{23}$$

where m is the mth iteration of step 7.

(8) The peripherally averaged Nusselt numbers are determined from equations (19) and (20).

(9) Steps 2–8 are repeated at the next axial location until the final z location is reached.

COMPUTATIONAL TESTS AND DETAILS

A uniform cross-sectional mesh size of 31×31 is used for the square channel. The full domain of the cross section is used since some asymmetric flow patterns are observed and will be discussed later. The axial step size Δz was varied from 10^{-5} near the duct entrance to about 2.56×10^{-3} near the fully developed region; about 130 forward steps are needed to reach the fully developed region. A grid independence test in the cross-sectional direction has been performed for a denser grid (46×46), at high rotational speed (i.e. $Re\ Re_\Omega = 10^4$, $Ro = 0.2$) which causes sharp velocity gradients. The predicted heat transfer and friction coefficients changed by less than 3 and 2% for values of z less than 7.7×10^{-4} and by lesser amounts for larger z. An exploratory run for a denser axial grid was performed by halving the axial step size, and the heat transfer and friction coefficients changed by less than 1.7 and 1.5% at all axial locations. As a partial verification of the computational procedure, the hydrodynamically developing flow was calculated without rotation. The results were compared with Shah and London [23] and Curr *et al.* [24]. The apparent friction factors were found to agree within 2% at all axial stations. Due to the lack of simultaneously developing flow data, the hydrodynamically fully developed flow with thermal development was obtained without rotation. The peripherally averaged Nusselt numbers were found to agree within 0.5% with Shah and London [23] and Chandrupatla and Sastri [25] for axial locations downstream of $z/Pr = 5 \times 10^{-3}$. Typical computation times on an IBM3090 computer were approximately 600–900 CPU seconds.

RESULTS AND DISCUSSION

In the presentation that follows, detailed results for low Ro and high Ro are given separately. Results for $Pr = 0.7$ and 7.0 are shown. Although presentation of the friction factor and Nusselt number in the entrance region is a major goal here, developments of velocities and temperature are also of interest and are useful in clarifying the heat transfer mechanisms. Information about the flow and temperature field developments are provided via vector plots of secondary flow and isotherm maps. Finally, a comparison of the present results with some experimental and numerical results is presented.

As shown in Fig. 1, a square channel is rotating at a constant speed about the X-axis. The fluid in the core region is driven in the negative Y-direction by the Coriolis force. The downward flow in the core region forces the fluid near the side walls to flow in the positive Y-direction and a pair of counter-rotating vortices is generated. These are so called 'Dean' type cells, similar to the curved pipe situation. The parameter $Re\ Re_\Omega$ used here is analogous to the Dean number, K, used for curved pipes. As shown in ref. [3], the relation is $Re\ Re_\Omega \sim K^2$. In the present numerical study an additional pair of vortices is observed near $X = a/2$ and $Y = 0$ in the high $Re\ Re_\Omega$ and moderate Ro regime, and changes in flow and heat transfer characteristics are also found. The two-pair vortex phenomenon is called 'vortex breakdown' in the present study. The vortex breakdown phenomenon, or roll cell instabilities, will now be discussed. During the past decade, a considerable amount of research has been conducted on the roll cell instabilities in pressure-driven channel flow with rotation [1, 2, 4–10]. The flow becomes unstable due to the local imbalance between the Coriolis force and the inertial force near the bottom wall [7]. The analyses reported before were all confined to the fully developed flow region. The axial dependence, or entrance effects, have never been investigated theoretically. The present calculation not only includes the entrance effect, but also will reveal that the behavior of the roll cell instabilities varies with z.

Figure 2 shows the secondary flow patterns and isotherm maps for a case without vortex breakdown at different axial locations. The parameters are $Re\ Re_\Omega = 5 \times 10^4$, $Ro = 0.2$, and $Pr = 0.7$ and 7.0. This choice of parameters represents a case in which the Coriolis force is significant.

Figure 2(a) demonstrates the secondary flow pattern at one axial location. This special location is chosen at $z = 1.533 \times 10^{-3}$, where the two 'Dean' type cells are clearly seen. The strong upward flow near the side walls is observed and this induces the Ekman layer [26]. A uniform downward secondary flow is observed in the core region, which has two effects. One is that the downward flow pushes the axial velocity peak downward, thereby increasing the local shear stress near the bottom wall. Another is that

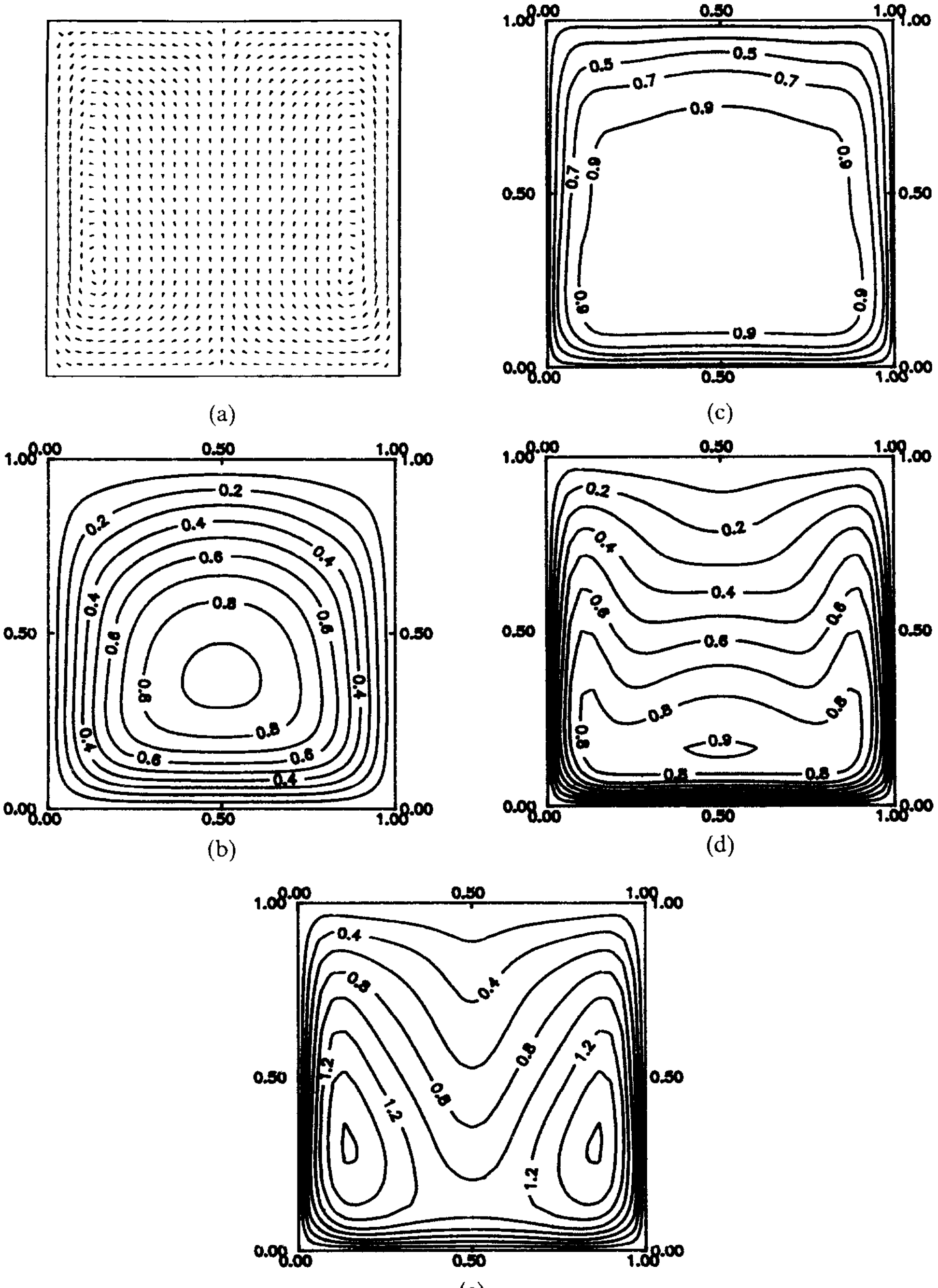

(a) (c)

(b) (d)

(e)

FIG. 2. Secondary flow and isotherm maps for $Re\,Re_{\Omega} = 5\times10^{4}$, $Ro = 0.2$: (a) secondary flow map at $z = 1.533\times10^{-2}$; (b) isotherm map for $Pr = 0.7$ at $z = 1.533\times10^{-2}$; (c) isotherm map for $Pr = 7.0$ at $z = 1.533\times10^{-2}$; (d) isotherm map for $Pr = 7.0$ at $z = 6.909\times10^{-2}$; (e) isotherm map for $Pr = 7.0$ at $z = 0.26877$ $(\theta\times10)$.

the downward secondary flow induces an upstream Coriolis force, which flattens the axial velocity profile.

The isotherm map for $Pr = 0.7$ is shown in Fig. 2(b) at the same axial location. It is observed that the isotherms are more sparsely spaced in the upper region of the cross section than in the lower region. Consequently, pronounced peripheral variations are expected in the local heat transfer.

Figures 2(c)–(e) are isotherm maps for $Pr = 7.0$. At $z = 1.533\times10^{-2}$ as shown in Fig. 2(c), the thermal boundary layer is fairly thin, compared to the $Pr = 0.7$ case. Further downstream at $z = 6.909\times10^{-2}$ a large temperature gradient is observed at the side and bottom walls; the reason for this is the large axial velocity gradients in these regions. The peak temperature core, $\theta = 0.9$, is shrinking to an eye shape near the bottom wall. The physical mechanisms can be described easily here; the larger upward secondary flow near the side wall brings the relatively 'cold' (i.e. non-dimensional temperature close to zero) fluid to the top wall, and the colder fluid near the top wall returns to the core region of the duct. Since the downward secondary flow in the core region is quite uniform, the flattened isotherms are expected. The temperature becomes fully developed around $z = 0.26877$ as shown in Fig. 2(e). Two symmetric 'high' temperature regions are observed. This is due to the cold fluid from the upper region flowing downward and isolating the warmer fluid in the two sides of the duct.

Figures 3(a)–(i) demonstrate a case in which vortex breakdown occurs. The parameters are $Re\, Re_{\Omega} = 5 \times 10^4$, $Ro = 10$, and $Pr = 0.7$ and 7.0, corresponding to a slower rotational speed than the previous case.

Figures 3(a)–(c) demonstrate the secondary flow patterns at three axial locations. Figure 3(a) shows the onset of the roll cell instability which leads to vortex breakdown. A pair of small counter-rotating vortices is found near the bottom of the centerline. This second pair of counter-rotating vortices are called 'eddies' throughout this paper in order to distinguish between the Dean type cells and the vortex breakdown induced cells. A fully developed two pair vortex pattern is then observed at axial location $z = 8.189 \times 10^{-2}$ as shown in Fig. 3(b). The second pair of counter-rotating vortices (eddies) is symmetric with respect to the y-axis. A strong upward secondary flow is found between these two eddies, and a strong downward secondary flow is observed between the large vortices and the small eddies. Finally, an asymmetric secondary flow pattern is observed in Fig. 3(c). The eddy on the right-hand side grows stronger and tends to envelop the eddy on the left-hand side. The center of the eddy on the right-hand side almost shifts to the centerline of the duct. This shifting behavior indicates the evolution of two vortex pairs back to one pair, which will be discussed later. Since the eddy on the left-hand side becomes weaker and smaller, the local velocity and temperature gradients between the eddy on the left-hand side and the bottom will decrease, thus a decrease in friction factor and heat transfer is expected. It is noted that the two pairs of counter-rotating vortices persist for quite a long distance (from $z = 0.06$ to around 0.23) before becoming asymmetric. A computation for a half domain would be meaningless beyond this point.

Figures 3(d)–(f) demonstrate the isotherm maps for $Pr = 0.7$. Figure 3(d) shows isotherms at an axial location $z = 3.069 \times 10^{-2}$. It is worth noting that the isotherms are slightly distorted upward near the center of the bottom wall. Similar behavior can also be seen in the isovel pattern at the same axial location (not shown). Figure 3(e) shows the isotherms affected by the roll cell instability. Two symmetric high temperature cores are found. Larger temperature gradients are also observed between each of the two high temperature cores and the bottom wall, thus a higher heat transfer rate is expected in this region. Finally, asymmetric isotherms are shown in Fig. 3(f). The mixing ability of the 'cold' fluid near the bottom wall to the 'hot'

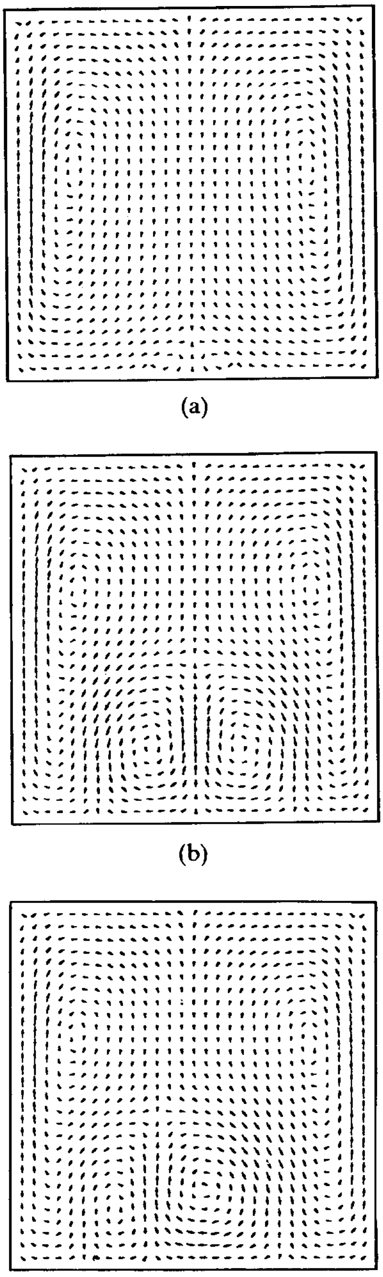

FIG. 3(a–c). Secondary flow and isotherm maps for $Re\, Re_{\Omega} = 5 \times 10^4$, $Ro = 10$: (a) secondary flow map at $z = 3.069 \times 10^{-2}$; (b) secondary flow map at $z = 8.189 \times 10^{-2}$; (c) secondary flow map at $z = 0.26877$.

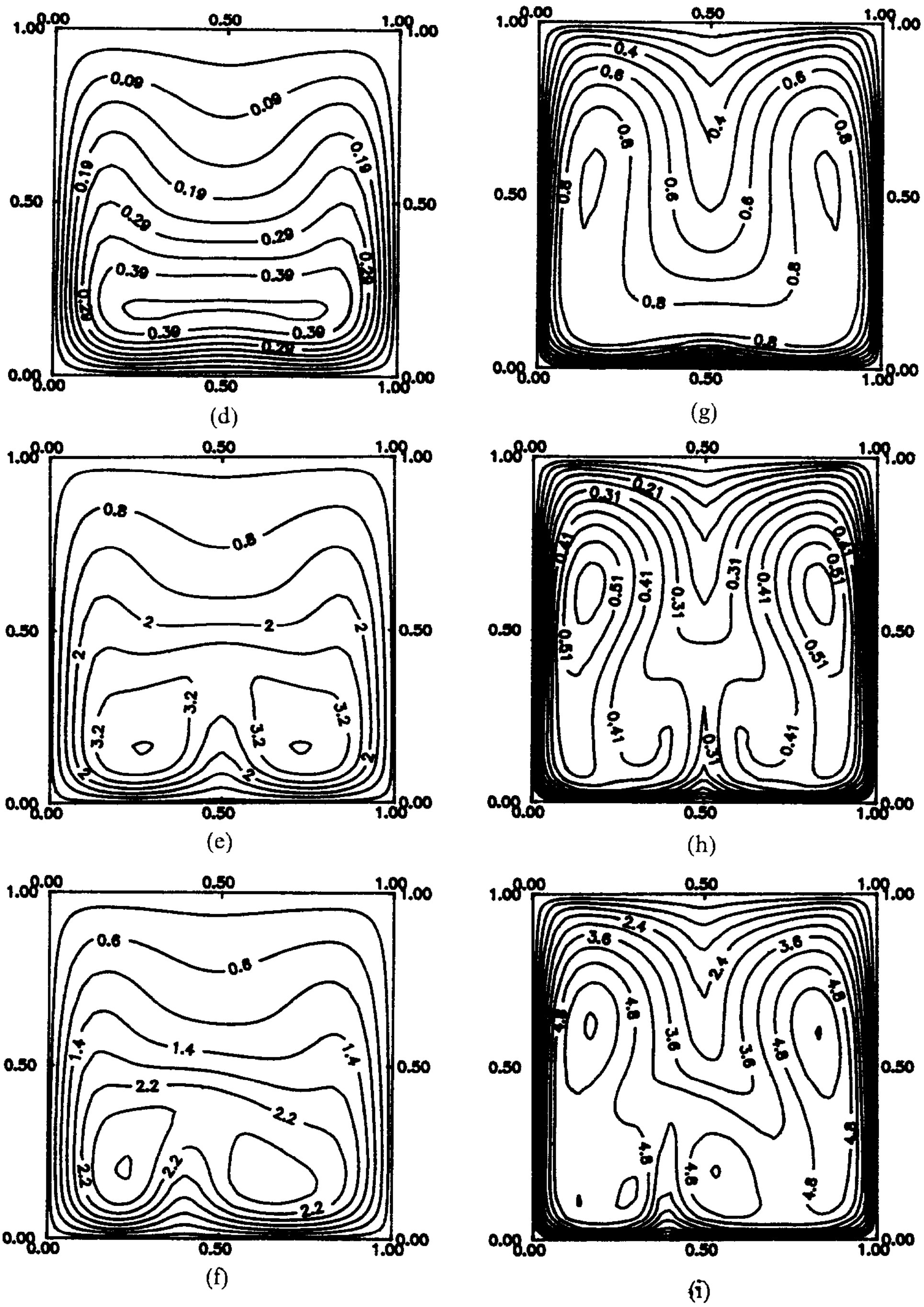

FIG. 3(d–i). (d) isotherm map for $Pr = 0.7$ at $z = 3.069\times10^{-2}$; (e) isotherm map for $Pr = 0.7$ at $z = 8.189\times10^{-2}$ ($\theta\times10^{2}$); (f) isotherm map for $Pr = 0.7$ at $z = 0.26877$ ($\theta\times10^{5}$); (g) isotherm map for $Pr = 7.0$ at $z = 3.069\times10^{-2}$; (h) isotherm map for $Pr = 7.0$ at $z = 8.189\times10^{-2}$; (i) isotherm map for $Pr = 7.0$ at $z = 0.26877$ ($\theta\times10^{2}$).

fluid region in the left-hand section is weaker because the eddy on the left-hand side is weaker. A higher temperature is therefore seen in the high temperature core on the left-hand side.

Figures 3(g)–(i) show the isotherms for $Pr = 7.0$ at three different locations. A typical U-shaped high temperature core is seen in Fig. 3(g). Two separated high temperature cores align symmetrically in the cross section, and the onset of instability begins to distort the isotherm near the center of the bottom wall. At $z = 8.189\times10^{-2}$ (Fig. 3(h)), the eddies have developed, thus significantly distorted isotherms are observed in the eddy region. Figure 3(i) demonstrates the asymmetric isotherm map at $z = 0.26877$. The high temperature core induced by the eddy on the right-hand side shifts significantly toward the left-hand side. The originally connected high temperature region on the right-hand side is now breaking into two separated regions. The high temperature core on the left-hand side induced by the eddy on the left-hand side seems to merge with the upper high temperature core.

DEVELOPMENT OF AXIAL VELOCITY PROFILES

The developing profiles of the axial velocity, w_1, along the line $x = 1/2$, are illustrated in Figs. 4(a) and (b). It is well known that the axial velocity profiles for pure forced convection without rotation are symmetric about the center axis of the square duct. With the effect of the Coriolis force, the shift of the velocity profiles becomes apparent. Figure 4(a) demonstrates the axial velocity profiles at different axial locations for parameters $Re\,Re_\Omega = 5 \times 10^4$, $Ro = 0.2$. The w profiles have been plotted at seven axial locations starting from very near the entrance of the square duct (curve A) to a location in the fully developed region (curve G). Near the inlet, the velocity profile is fairly uniform over the cross section as shown by curve A. As the flow develops (curves B–D), the axial velocity peak is displaced toward the bottom wall by the Coriolis force acting in the negative y-direction. Further downstream, at $z = 1.5 \times 10^{-2}$ (curve E), the Dean type cells have formed. The axial velocity peak is still toward the bottom of the duct, due to the downward secondary flow in the core. The Coriolis force acting in the upstream direction (cf. equation (9)) becomes stronger due to the stronger downward secondary flow, and a decrease in peak velocity is observed in curve F. Finally, a fully developed axial velocity profile is reached, as shown in curve G.

The case just presented in Fig. 4(a) showed the axial velocity development without vortex breakdown. A case with vortex breakdown is presented in Fig. 4(b). The vortex breakdown phenomenon is of importance in the fundamental research of roll cell instabilities, and it also changes the flow and heat transfer characteristics significantly. Figure 4(b) shows the axial velocity profiles at $x = 1/2$ for $Re\,Re_\Omega = 5 \times 10^4$ and $Ro = 10$. As before, curves A–C show the developing velocities in the inlet region. Since the Rossby number (representing the ratio of axial velocity and rotation speed) is large, the rotation speed is relatively small. This indicates that the Coriolis force induced by the y-direction secondary flow is small, thus the small increase in velocity gradient near the bottom wall is not noticeable in curves A–C. This indicates that the local shear stress increase near the bottom wall is negligible. Further downstream, at $z = 1.5 \times 10^{-2}$ (curve D), the Dean type cells are already established, and the distortion of axial velocity becomes apparent. A large velocity gradient is observed near the bottom wall, indicating large local shear stress. Further downstream, the onset of a second pair of eddies pushes the peak axial velocity toward the positive y-direction as shown in curves E–G. It is noted that the peak axial velocity becomes smaller from curve E to G. This is because the Coriolis force induced by the uniform secondary flow is in the upstream direction in the core region. Further downstream, at $z = 8.2 \times 10^{-2}$ (curve H), the second vortex pair has become completely established. The two vortex pairs persist for a long axial distance before evolving into one vortex pair. Curve I, at $z = 0.26877$, shows the axial velocity variations in the beginning of evolution from two vortex pairs to one vortex pairs. It is noted that a second axial velocity peak is observed at about $y = 0.2$. If we examine the asymmetric secondary flow pattern in the previous section (Fig. 3(c)), the center of the eddy on the right-hand side has shifted to about $y = 0.2$. Thus, there is no axial Coriolis force due to secondary flow at this point; the only Coriolis force is the one induced by the axial velocity, which acts in the negative y-direction.

AXIAL VARIATION OF THE FRICTION FACTOR AND THE NUSSELT NUMBER

The wall shear stress is presented in terms of the friction factor ratio $(f\,Re)/(f\,Re)_o$, where the subscript o denotes the quantity for fully developed pure forced convection. Figures 5(a) and (b) show the values of $(f\,Re)/(f\,Re)_o$ vs dimensionless axial distance z for the cases of $Ro = 10$, 1, 0.5, 0.2, and 0.1 with $Re\,Re_\Omega = 10^3$, 10^4, 5×10^4, and 10^5. The cases of $Re\,Re_\Omega = 10^3$, $Ro = 0.5$, 0.2 are not included because the graph becomes too cluttered and the case $Re\,Re_\Omega = 10^5$, $Ro = 0.1$ is excluded because an extremely long computation time is required to obtain the solution. Figure 5(a) presents the axial variation of $(f\,Re)/(f\,Re)_o$ for different $Re\,Re_\Omega$ with $Ro = 10$ and 1, which indicates a large to medium ratio of Re and Re_Ω. From the definitions of Re, Re_Ω, and Ro, it is seen that holding Ro fixed while increasing $Re\,Re_\Omega$ is like simultaneously increasing the Reynolds number Re and rotational Reynolds number Re_Ω at a fixed ratio of Re and Re_Ω. The curve of pure forced convection without rotation is denoted by curve A. Near the inlet, the Coriolis force is insignificant and all the curves in this figure follow the pure forced convection curve. Note that curve A (i.e. no rotation case) in the inlet region lies a little bit above the curves for the rotating cases. The authors believe that this is because of the numerical error due to the very small value of $Re\,Re_\Omega$ used to approximate the no rotation case. (Note that $Re\,Re_\Omega$ cannot be set exactly equal to zero with the nondimensionalization used here.) Comparing the present results for no rotation with Shah and London [23], the apparent friction factor in the present computations in the inlet region is found to be about 2% higher. Thus, accounting for this error,

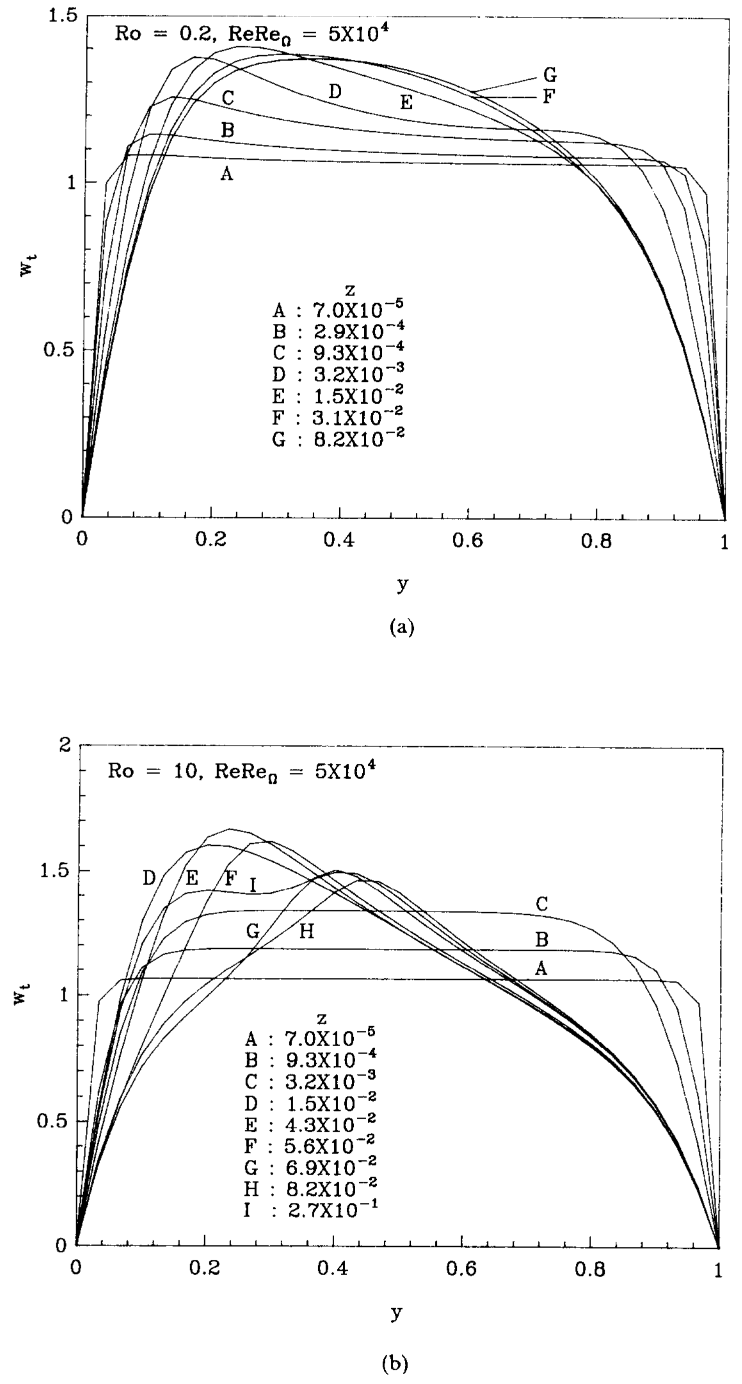

FIG. 4. Development of axial velocity profiles: (a) development of axial velocity along $x = 1/2$; (b) development of axial velocity along $x = 1/2$.

curve A is expected to follow the curves for large to medium Rossby number in the inlet region. As the Coriolis force becomes important, at about $z = 10^{-3}$ or later, the $(f\ Re)/(f\ Re)_o$ curves rise above the forced convection curve. The Coriolis induced secondary flow of Dean type cells plays a role in this region, which will be referred to as the 'rotational developing' flow region. In this region, the vortex pair grows stronger and stronger, and larger shear stresses are found at the side and bottom walls. Finally, a nominally constant friction factor is reached, which will be referred to as the fully developed flow region. For some cases, the vortex breakdown phenomenon is observed, and the increase in $(f\ Re)/(f\ Re)_o$ ratio

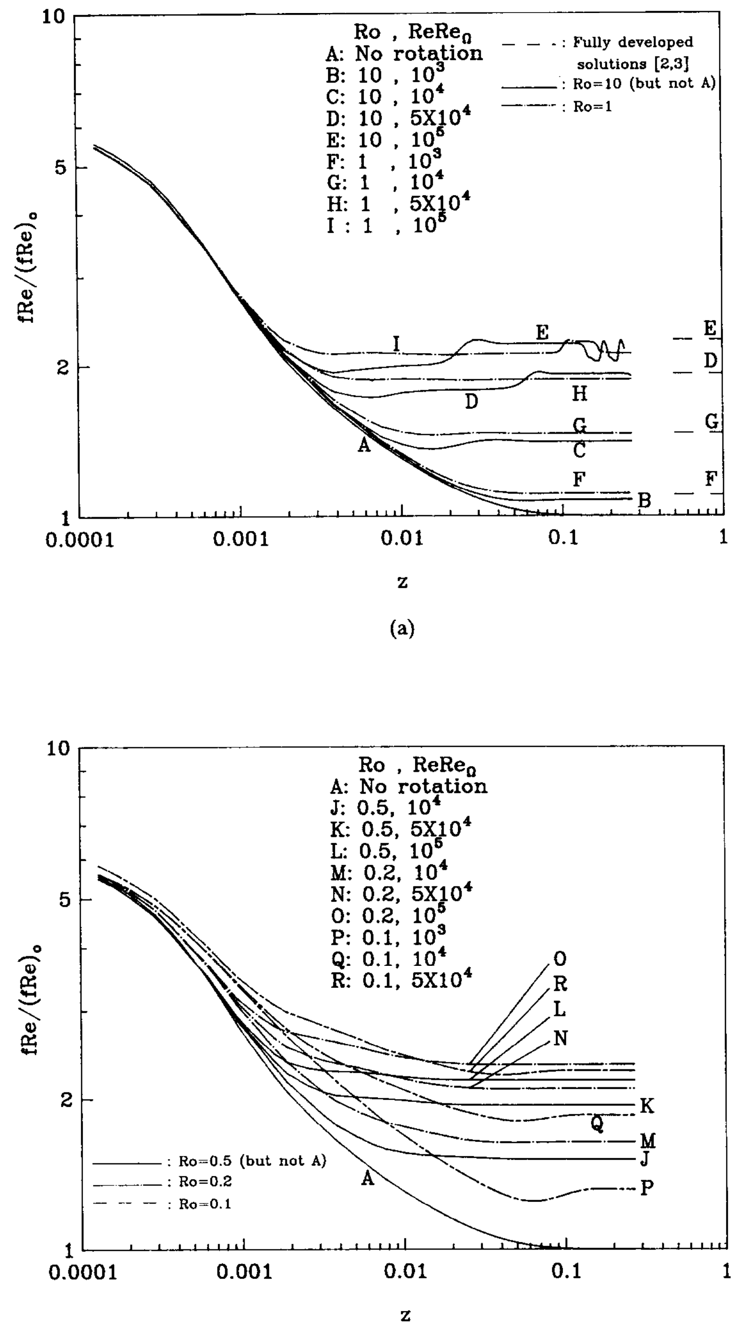

FIG. 5. $(f\ Re)/(f\ Re)_o$ vs z for various Ro and $Re\ Re_\Omega$ in a square channel: (a) friction factor ratio for $Ro = 10$ and 1; (b) friction factor ratio for $Ro = 0.5$, 0.2, and 0.1.

is significant. Curves B–E and curves F–I represent different $Re\ Re_\Omega$ values with $Ro = 10$ and 1, respectively. It is observed that the friction factor ratio increases with $Re\ Re_\Omega$ at a fixed value of Ro. It can also be seen that an order of magnitude change in $Re\ Re_\Omega$ has a stronger effect than an order of magnitude change in Ro. Generally, for fixed $Re\ Re_\Omega$, a higher value of Ro results in a smaller value of $(f\ Re)/(f\ Re)_o$ except when vortex breakdown occurs. The dashed lines at the far right indicating values of fully developed solutions are the results presented in refs. [1, 2] for the same cases. Excellent agreement is found; the worst case is for $Re\ Re_\Omega = 10^5$, $Ro = 10$, where about 1% error is observed. Note that curves E and

D for the fully developed cases correspond to two vortex pairs. Curve E demonstrates that the roll cell instabilities have an oscillatory behavior with z. It is seen that the two vortex pairs persist for a long distance, and at about $z = 0.11$, they evolve into one vortex pair, and strongly oscillatory behavior is observed further downstream. Curve D is also starting to evolve into a single vortex pair at the final axial location of the present calculations. Recall that detailed secondary flow and isotherm maps were presented in the previous section. It is interesting to see that curve I ($Re\,Re_\Omega = 10^5$ and $Ro = 1$) has a long distance with two vortex pairs, and no strongly periodic behavior is observed after evolving to one vortex pair at an axial location of about $z = 0.15$. It is worth noting, although not presented in the figures, that there exist two very small counter-rotating vortices near the centerline of the bottom wall even when the one pair solution dominates the secondary flow field. It is expected that the vortex breakdown phenomenon will appear again further downstream. It should be noted that the axial dependence of flow instabilities suggests that transient behavior may also exist in the flow field. Spezial and Thangan [7–9] in their constant pressure gradient calculations showed fully developed, time-independent, roll cell instability solutions. However, Jen recalculated the flow in a time dependent, full domain in a square duct with constant flow rate constraint, and found that the spatially periodic behavior of the roll cell instabilities was also time dependent. Therefore, transient effects should be taken into account in the region of vortex-breakdown. Further investigations are needed for transient effects, however, in the present calculations steady state behavior is assumed.

Figure 5(b) demonstrates the friction factor ratios for small values of Rossby number, which indicates larger Coriolis force effect relative to inertial effect, at various values of $Re\,Re_\Omega$. The quantity $(f\,Re)/(f\,Re)_0$ increases with $Re\,Re_\Omega$ at fixed Ro. For these small values of Ro, $(f\,Re)/(f\,Re)_0$ increases more with increasing $Re\,Re_\Omega$ closer to the inlet of the duct. The maximum increase in friction factor ratio for $z < 10^{-3}$ is about 5% relative to the no rotation case. Further downstream, in the 'rotational developing' flow region, the strong secondary flow of 'Dean' type cells causes the larger wall shear stress at the side and bottom walls. The increase in $(f\,Re)/(f\,Re)_0$ in this region is significant. In the fully developed flow region, the maximum increase in $(f\,Re)/(f\,Re)_0$ is over 150%. Note that in the large to moderate Rossby number (i.e. 10–0.5) range, the increase in friction factor ratio is negligible in the entrance region since the Coriolis force is not strong enough to substantially change the axial velocity profiles.

Figures 6(a), (b) and 7(a), (b) present the axial variation of Nusselt number for Prandtl numbers of 0.7 and 7.0, respectively. The increase in heat transfer in the inlet region due to the effect of rotation is insignificant as observed in Fig. 6(a). In the rotational developing flow region, starting at about $z/Pr = 10^{-3}$, the Nu curves rise above the no rotation case, and increase after reaching a minimum. The increase is due to the vortices which cause large temperature gradients close to the bottom and side walls. With an increase in $Re\,Re_\Omega$ at fixed Ro and Pr, the Nusselt number increases as was seen for the friction factor ratio. There are two parameters, $Re\,Re_\Omega$ and Ro, which affect the heat transfer coefficients at a fixed Prandtl number, or alternatively, Re and Ro. For a fixed value of $Re\,Re_\Omega$, it is easy to show that the larger Ro implies larger Re. It is shown in ref. [6] that the Reynolds number has a major effect on the heat transfer in the fully developed flow region. It is also demonstrated in the present study that near the fully developed region the Nusselt number increases with Rossby number at fixed $Re\,Re_\Omega$. A significant increase in Nu is observed when the vortex breakdown phenomenon occurs. The maximum increase in heat transfer due to rotation in this figure compared to the no rotation case is over 400%, as shown in curve E, at axial location $z/Pr = 4 \times 10^{-2}$. Excellent agreement of Nu in the fully developed region is found in comparison with refs. [1, 2], except for the case of $Re\,Re_\Omega = 10^5$, $Ro = 1$ (curve I). Since dual solutions were obtained in refs. [1, 2] for this special case, the two solutions are shown in line I. The upper line is the solution for two vortex pairs, and the lower line is one vortex pair. The difference between the two solutions is 3%.

Figure 6(b) presents Nu for small Rossby number, or strong rotation effect. It is observed that the increase of Nusselt number is still negligible in the inlet region. Although the strong Coriolis force increases the local wall shear stress near the bottom wall, the thermal boundary layer is too thin to be affected by the distorted axial flow field in the inlet region.

It is to be expected that the rotational effect is also negligible for larger Pr in the inlet region. Figures 7(a) and (b) show the results for $Pr = 7.0$. It is observed that the rotation effect is insignificant in the inlet region, as shown in Fig. 7(a). The axial location at which Nu rises above the no rotation case strongly depends on the value of $Re\,Re_\Omega$. The axial locations vary from $z/Pr = 2 \times 10^{-4}$ to 1.5×10^{-3} as $Re\,Re_\Omega$ decreases from 10^5 to 10^3. The increase in Nu in the rotational developing region is again observed. The increase of Nu is significant in comparison with the $Pr = 0.7$ fluid in the rotational developing and fully developed flow regions. The general rule that Nu increases as $Re\,Re_\Omega$ increases at fixed Rossby number still holds. The significance of vortex breakdown in increasing the Nusselt number is also seen in this figure.

Figure 7(b) demonstrates the effect of small Rossby number for the $Pr = 7.0$ fluid. The increase in Nu in the inlet region is somewhat stronger than in Fig. 7(a). In the rotational developing region, the increase in Nu is significant. For curve O, the maximum increase in the fully developed region is over 500%.

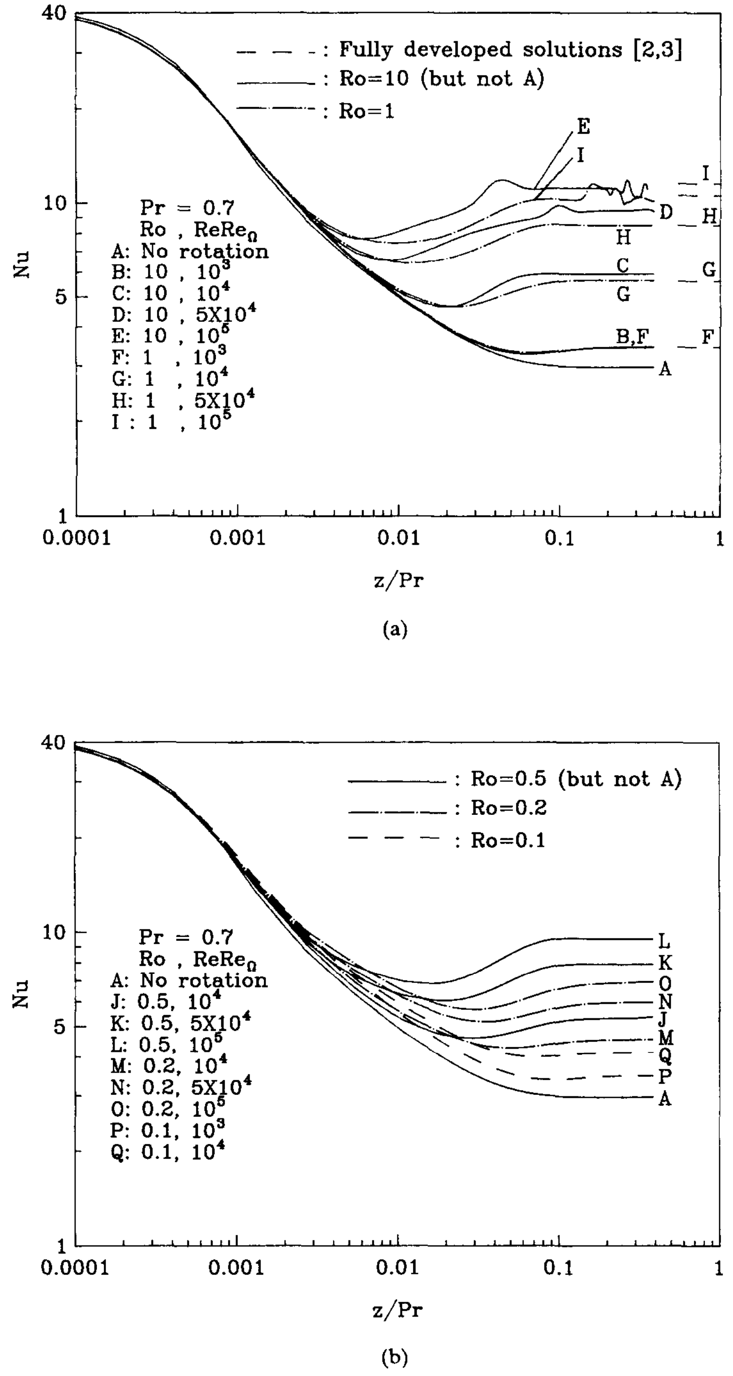

FIG. 6. *Nu* vs *z/Pr* for $Pr = 0.7$ fluid in a square channel: (a) Nusselt number for $Ro = 10$ and 1; (b) Nusselt number for $Ro = 0.5$, 0.2, and 0.1.

COMPARISON WITH EXPERIMENTAL RESULTS

Because of the lack of experimental data both in the fully developed and developing region of an isothermal rectangular duct, the present numerical computation is compared with the only existing square duct data [14, 15] at $L/D = 30$. Figure 8 shows the values of Nu_m vs $Re\ Re_\Omega$ (where Nu_m is the average up to $L/D = 30$). The data for $Re = 720$ lie very close to the present numerical solutions, and show almost the same trend as $Re\ Re_\Omega$ increases, except for the last data point. It was explained by Soong *et al.* [15] that this sudden decrease in mean Nusselt number is the

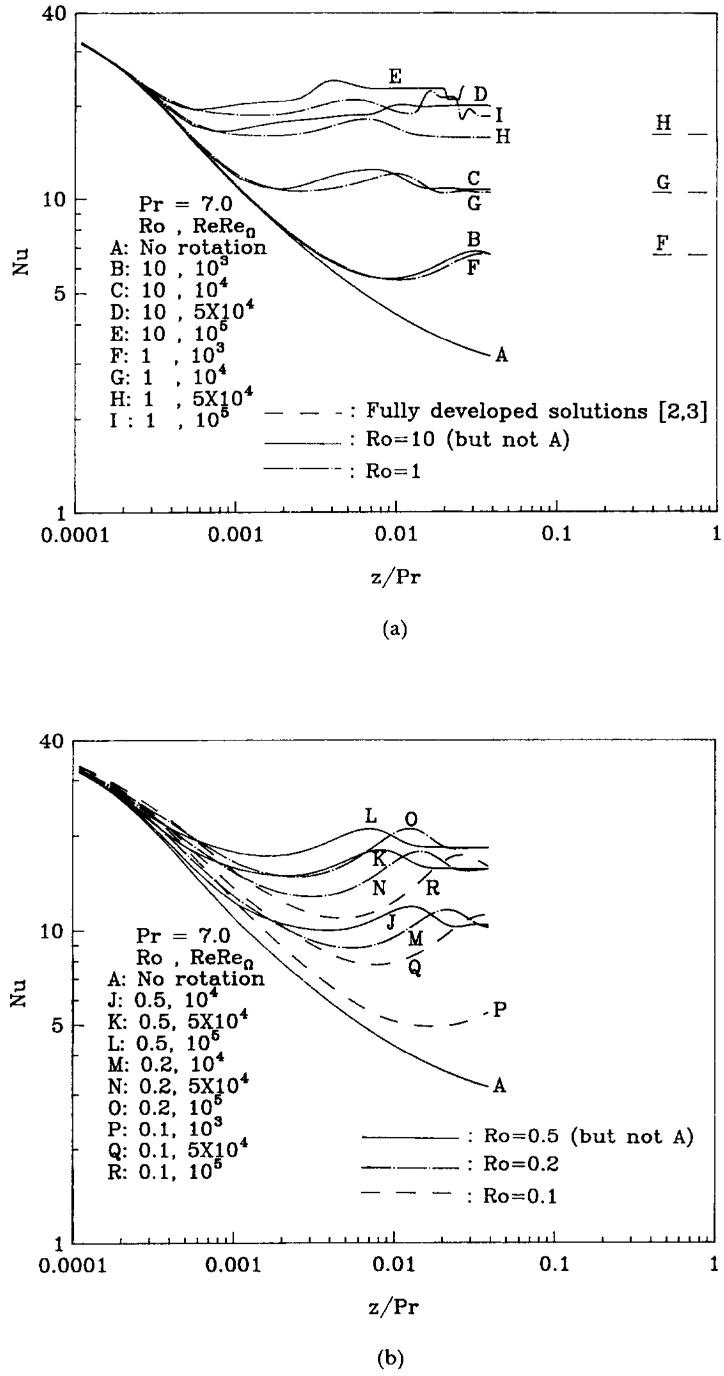

(a)

(b)

FIG. 7. *Nu* vs *z/Pr* for *Pr* = 7.0 fluid in a square channel: (a) Nusselt number for *Ro* = 10 and 1; (b) Nusselt number for *Ro* = 0.5, 0.2, and 0.1.

effect of the centrifugal-buoyancy force. The agreement is generally within 10% except the first point, which differs by 12.5%. The data for higher Reynolds numbers show larger discrepancies between numerical and experimental data. This may be due to the unknown inlet condition as indicated by Mori and Nakayama [11]. They compared their stationary duct heat transfer data to a numerical solution for thermally developing flow in a square duct, and found the experimental data to be higher except at low Reynolds number (i.e. $Re < 720$). This indicates that the experimental data may have entrance swirling or local turbulence effects which will increase heat transfer coefficients substantially in the entrance region,

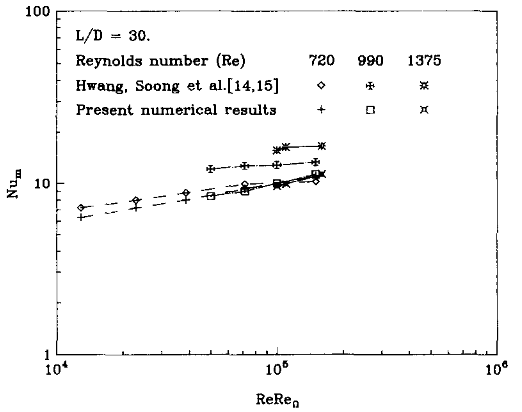

FIG. 8. Comparison of Nu_m with experimental data.

although the flow may relaminarize further downstream.

CONCLUDING REMARKS

(1) The equations governing the simultaneously developing laminar forced convection in the entrance region of a rotating isothermal square duct have been solved using a three-dimensional parabolic computational technique. A relatively novel vorticity–velocity method along with the power law scheme successfully solved the parabolized Navier–Stokes equations and energy equation. The solutions have been presented for Prandtl numbers of 0.7 and 7.0.

(2) The increases in $(f\ Re)/(f\ Re)_0$ ratios are significant both in the rotational developing and fully developed regions.

(3) The increase of Nu is small in the inlet region, since the thermal boundary layer is still too thin to be affected by the distortion of the axial flow induced by the Coriolis force. The rotational developing region is much longer than the inlet region. In practical applications, the flow remains in the thermally rotational developing region for almost the full length of the duct, and the Nusselt number in this region is lower than in the fully developed region. It is therefore essential not to use fully developed heat transfer results in designing rotating machinery. In comparison with the no rotation case, the increases in Nu are significant both in the rotational developing and fully developed flow regions. The maximum increases in these two regions is about 400% for the fluid of Prandtl number 0.7. The higher Prandtl number shows a maximum increase of 500% in the fully developed flow region.

(4) The vortex breakdown, or roll cell instability, phenomenon is observed. The increases in friction factor ratio and heat transfer coefficients are significant. The roll cell instability behavior varies in the axial direction.

(5) Generally speaking, the values of $(f\ Re)/(f\ Re)_0$ and Nu increase with the parameter $Re\ Re_\Omega$.

(6) Excellent agreement is found with numerical results in the fully developed region, for both friction factor ratio and Nusselt number. Comparisons with experimental results show reasonably good agreement for the mean Nusselt number at low Reynolds number. The discrepancy for higher Reynolds number may be due to the unknown inlet condition.

(7) The solutions presented here serve as useful data and provide insight into the complex interaction between fluid flow and heat transfer in the entrance region of rotating isothermal square ducts.

REFERENCES

1. G. J. Hwang and T. C. Jen, Convective heat transfer in rotating isothermal ducts, *Int. J. Heat Mass Transfer* **33**, 1817–1828 (1990).
2. T. C. Jen, Convective heat transfer in rotating isothermal rectangular ducts, M.S. Thesis, National Tsing Hua University, Hsinchu, Taiwan (1987).
3. G. J. Hwang and T. C. Jen, Forced laminar convection in fully developed flow in a rotating isothermal duct with the effect of axial conduction, *Proc. 1987 ASME/JSME Thermal Engng Joint Conf.*, Vol. 2, pp. 43–49 (1987).
4. J. E. Hart, Instability and secondary motion in rotating channel flow, *J. Fluid Mech.* **45**(2), 341–351 (1971).
5. D. K. Lezius and J. P. Johnston, Roll-cell instabilities in rotating laminar and turbulent channel flows, *J. Fluid Mech.* **77**(1), 153–175 (1976).
6. T. C. Jen and G. J. Hwang, Fully developed laminar convection in rotating isothermal isosceles triangular channels with the effect of axial conduction (in preparation).
7. C. G. Spezial, Numerical study of viscous flow in rotating rectangular ducts, *J. Fluid Mech.* **122**, 251–271 (1982).
8. C. G. Spezial and S. Thangan, Numerical study of secondary flow and roll-cell instabilities in rotating channel flow, *J. Fluid Mech.* **130**, 377–395 (1983).
9. C. G. Spezial, The effect of the earth's rotation on channel flow, *Trans. ASME* **53**, 198–202 (1986).
10. E. M. Smirnov, Bifurcation of developed flow in rectangular channels rotating about the transverse axis, *Izv. Akad. Nauk. SSSR. Mekh. Zhidk. Gaza* No. 5, 27–32 (1985).
11. Y. Mori and W. Nakayama, Secondary flows and enhanced heat transfer in rotating pipes and ducts. In *Heat and Mass Transfer in Rotating Machinery* (Edited by D. E. Metzger and N. H. Afgan), pp. 3–24. Research Studies Press, England (1984).
12. D. E. Metzger and R. L. Stan, Entry region heat transfer in rotating radial tubes, AIAA 15th Aerospace Science Meeting, pp. 77–89 (1977).
13. D. Skiadaressis and D. B. Spalding, Heat transfer in ducts rotating around a perpendicular axis, ASME Paper No. 77-WA/HT-39 (1977).
14. G. J. Hwang and C. Y. Soong, Experimental automation and heat transfer measurement on a rotating thermal system, *Proc. 3rd Int. Symp. on Transport Phenomena in Thermal Control*, pp. 665–678 (1988).
15. C. Y. Soong, S. T. Lin and G. J. Hwang, An experimental study of convective heat transfer in radially rotating rectangular ducts. In *Collected Papers in Heat Transfer 1989*, ASME HTD-Vol. 120.
16. S. V. Patankar, *Numerical Heat Transfer and Fluid Flow*. Hemisphere, Washington, DC (1980).
17. K. Ramakrishna, S. G. Rubin and P. K. Khosla, Laminar natural convection along vertical square ducts, *Numer. Heat Transfer* **5**, 59–79 (1982).
18. F. C. Chou and G. J. Hwang, Vorticity–velocity method for the Graetz problem and the effect of natural convection in a horizontal rectangular channel with uniform wall heat flux, *J. Heat Transfer* **109**, 704–710 (1987).

19. F. C. Chou and G. J. Hwang, Numerical analysis of the Graetz problem with natural convection in a uniformly heated horizontal tube, *Int. J. Heat Mass Transfer* **31**, 1299–1308 (1988).
20. C. G. Spezial, On the advantages of vorticity–velocity formulation of the equations of fluid dynamics, *J. Comput. Phys.* **73**, 476–480 (1987).
21. D. A. Anderson, J. C. Tannehill and R. H. Pletcher, *Computational Fluid Dynamics and Heat Transfer.* McGraw-Hill, New York (1984).
22. S. V. Patankar and D. B. Spalding, A calculation procedure for heat, mass and momentum transfer in three-dimensional parabolic flows, *Int. J. Heat Mass Transfer* **15**, 1787–1806 (1972).
23. R. H. Shah and A. L. London, *Laminar Flow Forced Convection in Ducts.* Academic Press, New York (1978).
24. R. M. Curr, D. Sharma and D. G. Tatchell, Numerical prediction of some three-dimensional boundary layers in ducts, *Comput. Meth. Appl. Mech. Engng* **1**, 143–158 (1972).
25. A. R. Chandrupatla and V. M. K. Sastri, Laminar forced convection heat transfer of a non-Newtonian fluid in a square duct, *Int. J. Heat Mass Transfer* **20**, 1315–1324 (1977).
26. E. M. Smirnov, Asymptotic drag formulas for the rapidly rotating radial channels of rectangular cross section, *Izv. Akad. Nauk. SSSR. Mekh. Zhidk. Gaza* No. 6, 42–49 (1978).

DEVELOPPEMENTS SIMULTANES DE LA CONVECTION LAMINAIRE DANS DES CONDUITS TOURNANTS A SECTION CARREE ISOTHERME

Résumé—On présente une analyse numérique de la convection laminaire forcée dans la région d'entrée d'un conduit isotherme à section carrée, tournant autour d'un axe perpendiculaire à l'axe du conduit. On examine le cas de l'établissement de l'écoulement. Trois paramètres indépendants sont introduits : le nombre de Prandtl (Pr), un nombre de Reynolds combiné à un autre rotationnel ($Re \cdot Re_\Omega$) et un nombre de Rossby (Ro). Une méthode vorticité–vitesse, relativement nouvelle, est utilisée avec le schéma de la loi-puissance. On présente les établissements typiques de la vitesse longitudinale, de l'écoulement secondaire et de la température en différentes positions axiales dans la région d'entrée. On présente aussi une comparaison des résultats numériques avec des données expérimentales.

ENTWICKLUNG EINER LAMINAREN KONVEKTIONSSTRÖMUNG IN ROTIERENDEN ISOTHERMEN QUADRATISCHEN KANÄLEN

Zusammenfassung—Die laminare erzwungene Konvektion im Eintrittsgebiet eines isothermen quadratischen Kanals, welcher um eine senkrecht zur Kanalachse stehende Achse rotiert, wird numerisch untersucht. Dabei interessiert der Fall einer sich simultan entwickelnden Strömung. Es werden drei unabhängige Parameter eingeführt: Prandtl-Zahl (Pr), das Produkt der Reynolds-Zahl mit der Reynolds-Zahl für die Rotationsbewegung ($Re\ Re_\Omega$) und die Rossby-Zahl (Ro). Bei der numerischen Untersuchung wird ein verhältnismäßig neues Wirbelgeschwindigkeits-Verfahren zusammen mit Potenzansätzen angewandt. Es werden die typischen Entwicklungen der Axialgeschwindigkeit, der Sekundärströmung und der Temperatur an unterschiedlichen axialen Positionen im Eintrittsgebiet vorgestellt. Ergebnisse für den örtlichen Reibungsbeiwert und die Nusselt-Zahl werden gezeigt, außerdem ein Vergleich der numerischen Ergebnisse mit verfügbaren Versuchsdaten.

ЛАМИНАРНАЯ КОНВЕКЦИЯ, РАЗВИВАЮЩАЯСЯ ПРИ ВРАЩЕНИИ ИЗОТЕРМИЧЕСКИХ КАНАЛОВ КВАДРАТНОГО СЕЧЕНИЯ

Аннотация—Проводится численный анализ ламинарной вынужденной конвекции во входном участке изотермического канала квадратного сечения, вращающегося вокруг оси, перпендикулярной оси канала. Исследуется случай с совместно развивающимся течением. Вводятся три независимых параметра: число Прандтля Pr, комбинированное и вращательное числа Рейнольдса $Re\ Re_\Omega$, а также число Россби Ro. В анализе используется относительно новый метод "скорость–завихренность" наряду со схемой степенного закона. Представлены типичные поля аксиальной скорости, вторичного течения и температуры при различных положениях по оси во входной области. Описываются изменения локального коэффициента трения и числа Нуссельта. Полученные численные результаты сравниваются с имеющимися экспериментальными данными.